Available online at www.sciencedirect.com
SCIENCE DIRECT
Catalysis Today 105 (2005) 162–172
CATALYSIS TODAY
www.elsevier.com/locate/cattod

Is the water–gas shift reaction on Pt simple? Computer-aided microkinetic model reduction, lumped rate expression, and rate-determining step

A.B. Mhadeshwar, D.G. Vlachos *

Department of Chemical Engineering and Center for Catalytic Science and Technology, University of Delaware, Newark, DE 19716-3110, USA

Available online 31 May 2005

Abstract

The water–gas shift (WGS) is an essential process in hydrogen production from hydrocarbon and biomass fuel processing. Recently, it was shown that the chemistry of the WGS reaction on Pt is complex and depends critically on the oxidation of CO by adsorbed OH and H_2O, mainly via the carboxyl intermediate [A.B. Mhadeshwar, D.G. Vlachos, J. Phys. Chem. B 108 (2004) 15246]. On the other hand, previous one-step rate expressions in the literature have described experimental data reasonably well. Here, starting from a comprehensive microkinetic model, we derive a reduced microkinetic model consisting of elementary reaction steps using principal component analysis and then develop a one-step rate expression for WGS on Pt using a posteriori analysis. It is shown that the rate-determining step of WGS on Pt is the oxidation of CO by H_2O, but the effective reaction rate constant and reaction orders are concentration dependent. Finally, the effect of uncertainty in reaction rate constants on the rate-determining step is discussed.

Keywords: Water–gas shift; Fuel processing; Fuel cells; Hydrogen; Platinum; Thermodynamic consistency; Model reduction; Sensitivity analysis; Reaction path analysis; Principal component analysis; Rate-determining step

1. Introduction

Widespread commercialization of proton exchange membrane (PEM) fuel cells will critically depend on our ability to convert syngas, gasoline, diesel, and biomass into hydrogen, in an efficient, cheap, and environmentally benign way. Hydrogen is typically produced from syngas, which contains a large fraction of carbon monoxide. The water–gas shift (WGS) reaction is a typical process used for reducing the CO content to a low level, with the resulting stream being further processed in a preferential oxidation (PROX) reactor or by using membranes. The overall WGS reaction is represented as:

$$CO + H_2O \leftrightarrow CO_2 + H_2,$$
$$\Delta H = -41.2\,\text{kJ/mol at } 300\,\text{K}.$$

The WGS reaction is reversible and exothermic, so it is unfavorable at high temperatures. Typically, the reaction is carried out in multiple catalytic stages to increase the CO conversion. High temperature WGS shift (HTS) is carried out at ~310–450 °C on Fe/Cr catalysts, close to equilibrium conditions, where the reverse water–gas shift (RWGS) reaction also becomes important. This reduces the CO content in the fuel stream from ~10 to ~3% [1]. In order to increase the CO conversion, low temperature WGS shift (LTS) is subsequently carried out at ~160–250 °C on Cu/Zn oxide catalysts [1]. The catalysts in the second stage must be more active than those in the first stage, since the process is kinetically controlled at lower temperatures.

A major disadvantage of Cu based catalysts is their pyrophoric nature and deactivation in the presence of air and condensed water. Hence, there has been an increasing interest in noble metal catalysts that are non-pyrophoric and are highly active [2–13]. In a recent paper by Wheeler et al. [2], the performance of various noble metal catalysts and the

* Corresponding author. Tel.: +1 302 831 2830; fax: +1 302 831 1048.
E-mail address: vlachos@che.udel.edu (D.G. Vlachos).

0920-5861/$ – see front matter © 2005 Elsevier B.V. All rights reserved.
doi:10.1016/j.cattod.2005.04.003

effect of ceria promoter were studied at short contact time conditions. Such catalysts were found to show high WGS activity, stability, and performance. Furthermore, since short contact time reactors require less amount of catalyst than conventional reactors, the overall cost of using noble metals is partially offset. Cost may also not be the most critical issue for onboard reformers, used for example in portable power generation devices.

Modeling of WGS reactors requires detailed information of the underlying chemical kinetics. Typical sets of a WGS reaction mechanism include the CO oxidation, the H_2 oxidation, and coupling reactions between CO and H_2. Recently, we proposed such a detailed, elementary-like, thermodynamically consistent microkinetic model for water-promoted CO oxidation, WGS, and PROX on Pt [14]. An important finding from that work is that the carboxyl ($COOH^*$) intermediate and its associated formation and consumption reaction steps are key components in the WGS reaction. The proposed mechanism (see Table 1 in Ref. [14]) consists of 10 species and 46 irreversible reactions. Implementation of such large reaction mechanisms in reactor design or conduction of parametric studies using computational fluid dynamics (CFD) is a CPU demanding task [15]. Simpler mechanisms or rate expressions are easier to implement and faster to run, provided they are sufficiently accurate. Recent examples of application of simple rate expressions in CFD are given in [15–17].

Rate parameters estimated for different noble metal catalysts by Wheeler et al. [2] gave very good fits to the data using a simple one-step rate expression. A number of simple rate expressions and reaction orders have also been previously proposed in the literature and some of them are summarized in Table 1. In most cases, the assumed rate expression is the same (e.g., a power law expression) and irreversible, so its applicability is limited to non-equilibrium conditions. In some cases, reversible expressions have also been proposed. The orders of reactants and products vary significantly in some studies. The reasonable performance of the empirical one-step rate expressions indicates that the underlying WGS chemistry is possibly simple. Yet, our detailed modeling indicates that the $COOH^*$ chemistry is crucial [14].

In order to reconcile the partial success of one-step rate expressions given the inherent complexity of the actual chemistry, in this paper, we analyze the WGS reaction mechanism of [14]. We employ a systematic chemistry reduction methodology proposed earlier by our group [15,18] to first derive a reduced, microkinetic model and then attempt to obtain a one-step rate expression by a posteriori analysis of this reduced microkinetic model. Finally, the rate-determining step (RDS) is identified and effective reaction orders are discussed. An uncertainty analysis regarding the RDS is also briefly discussed.

2. General methodology for mechanism reduction

A hierarchical approach for mechanism development and optimization has previously been described in Ref. [16]. Here, we briefly discuss the overall methodology for mechanism reduction of comprehensive microkinetic models. A significant departure from previous work is that our approach is based on a posteriori analysis of the full microkinetic model results as compared to a priori assumptions typically employed in the literature. Our approach, depicted in Fig. 1, consists of the following steps.

Table 1
Summary of literature rate expressions and reaction orders for the WGS reaction on different catalysts

Catalyst	Rate expression	Reaction orders, α: CO, β: H_2O, γ: CO_2, δ: H_2	Ref.
α-Fe_2O_3	$r = kP_{CO}^{\alpha}P_{H_2O}^{\beta}$	$\alpha = 0.8$, $\beta = 0.08$	[28]
Fe/Al_2O_3	$r = kP_{CO}^{\alpha}P_{H_2O}^{\beta}$	$\alpha = 0.58$, $\beta = 0.04$	[29]
Cu(1 1 1)	$r = kP_{CO}^{\alpha}P_{H_2O}^{\beta}$	$\alpha = 0.5$–1, $\beta = 0$	[30]
Pt/CeO_2	$r = \frac{k_1k_2P_{CO}P_{H_2O}}{k_1P_{CO}+k_2P_{H_2O}}$	$\alpha = 1$, $\beta = 0$ for excess H_2O	[27]
Cu- and Ni-loaded CeO_2	$r = \frac{k_1k_2P_{CO}P_{H_2O}}{k_1P_{CO}+k_2P_{H_2O}}$	$\alpha = 1$, $\beta = 0$ for excess H_2O; $\alpha = 0$, $\beta = 1$ for excess CO	[31]
Pd/CeO_2	$r = kP_{CO}^{\alpha}P_{H_2O}^{\beta}P_{CO_2}^{\gamma}P_{H_2}^{\delta}$	$\alpha = 0$, $\beta = 0.5$, $\gamma = -0.5$, $\delta = -1$	[5]
Rh/CeO_2	$r = kP_{CO}^{\alpha}P_{H_2O}^{\beta}$	$\alpha = 0$, $\beta = 1$	[4]
Fe_3O_4/Cr_2O_3	$r = kP_{CO}^{\alpha}P_{H_2O}^{\beta}$	$\alpha = 1$, $\beta = 0$	[1]
Fe_3O_4/Cr_2O_3	$r = kP_{CO}^{\alpha}P_{H_2O}^{\beta}P_{CO_2}^{\gamma}P_{H_2}^{\delta}(1-\mu)$	$\alpha = 1.1$, $\beta = 0.53$, $\gamma = 0$, $\delta = 0$	[32]
Cu-based	$r = kP_{CO}^{\alpha}P_{H_2O}^{\beta}P_{CO_2}^{\gamma}P_{H_2}^{\delta}\left[1-\frac{P_{CO_2}P_{H_2}}{K_{eq}P_{CO}P_{H_2O}}\right]$	$\alpha = 0.8$, $\beta = 0.8$, $\gamma = -0.7$, $\delta = -0.8$	[33]
(i) V, Nb-based and Ca, Ni-based	$r = kP_{CO}^{\alpha}P_{H_2O}^{\beta}$	(i) $\alpha = 0.5$, $\beta = 0.5$	[34]
(ii) Li, Mg-based		(ii) $\alpha = 0$, $\beta = 0.5$	
Noble metal/ceria supported noble metals	$r = kP_{CO} - \frac{k}{K_{eq}}P_{CO_2}$	$\alpha = 1$, $\beta = 0$ for excess H_2O and H_2	[2]
Pt based catalysts	$r = \frac{k_{33}K_{19}K_{13}C_{CO}C_{H_2O}-k_{34}K_{21}K_1K_{31}^{-1}C_{CO_2}C_{H_2}}{(1+\sqrt{K_1C_{H_2}}+K_{19}C_{CO})^2}$	$\alpha = -1$:1, $\beta = 0$:1, $\gamma = 0$:1, $\delta = 0$:1	This work

k, r, P, and μ stand for rate constant, rate, partial pressure, and reversibility factor, respectively.

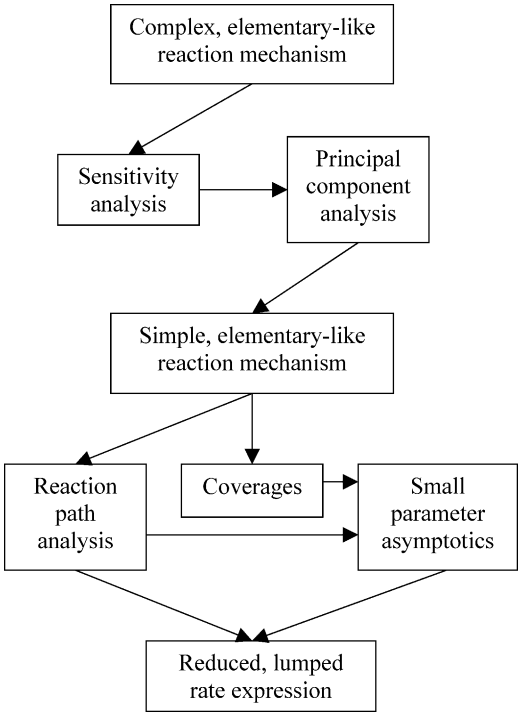

Fig. 1. Flow chart of the mechanism reduction methodology.

2.1. From complex mechanisms to reduced, elementary-like mechanisms

The first step in mechanism reduction is to identify the important reaction steps. Sensitivity analysis (SA) is performed for selected model response(s) (R) with respect to rate parameters. Typical model responses can be reactant conversion, product selectivity, reaction rate, species mass fractions, etc. In this work, we have chosen the pre-exponentials (A) as parameters and the species mass fractions at different temperatures as the model responses. A pairwise perturbation is carried out, i.e., both the forward and the backward pre-exponentials are simultaneously perturbed by the same factor in order to keep the equilibrium constant fixed that in turn maintains thermodynamic consistency. The elements of the normalized sensitivity matrix $\mathbf{S}$ are defined as

$$S_{ij} = \frac{\partial(\ln R_i)}{\partial(\ln A_j)}. \quad (1)$$

Next, principal component analysis (PCA) is carried out using the SA information. PCA has been proposed as an eigenvalue–eigenvector decomposition of sensitivity matrices that can reveal synergetic interactions among chemical reactions [19,20]. This is an important step especially when multiple conditions, e.g., several temperatures and compositions, are simultaneously analyzed to reduce a mechanism over a wide range of conditions. Briefly, the matrix $\mathbf{S}^T\mathbf{S}$ is computed (the superscript T denotes the transpose of the sensitivity matrix $\mathbf{S}$) and its eigenvalues and eigenvectors are computed using Matlab. The dominant eigenvalues indicate the most important eigenvectors, and the biggest-in-magnitude elements of these important eigenvectors indicate the most important reactions in the mechanism for the selected model response(s). This procedure results in a reduced reaction mechanism, while maintaining the elementary-like nature of chemical reactions.

2.2. From reduced, elementary-like mechanisms to an analytical rate expression

Starting from a reduced reaction mechanism consisting of elementary-like reactions, reaction path analysis (RPA) is performed to identify the contribution of different reactions to the species balances. Using small parameter asymptotics (in mathematical asymptotics' terminology, this is an order O(1) approach), relatively small rates in species balances as well as small coverages in site balances are omitted based on pre-set thresholds. This step naturally identifies partial equilibrium (PE) conditions, most abundant reaction intermediates (MARI), and the RDS(s). An analytical rate expression is then derived at steady state from the set of algebraic equations consisting of simplified species and site balances. The validity of the analytical rate expression is then checked. If necessary, the thresholds are adjusted to control accuracy and algebraic complexity. Next, we apply this multistep methodology to the WGS reaction on Pt.

3. The water–gas shift reaction on Pt

3.1. Full reaction mechanism and comparison to experimental data

Recently, we proposed an elementary-like comprehensive surface reaction mechanism (10 species and 46 reactions) for water promoted CO oxidation, WGS, and PROX on Pt [14]. The subsets of WGS chemistry, viz. the CO oxidation [21] and the H_2 oxidation [14] were first optimized. The two mechanisms share only O^* as a common oxidizer. However, in mixtures of CO and H_2, OH^* becomes a crucial common intermediate formed by H_2O dissociation and H_2O is also present, therefore, additional coupling reactions need to be accounted for. It was found that the predicted catalyst activity is drastically reduced when these additional CO–H_2 coupling steps are not taken into account. Specifically, the following paths of CO oxidation to CO_2

$$CO^* + OH^* \leftrightarrow CO_2^* + H^* \quad (\text{direct path to } CO_2, R_{26}-R_{25})$$

$$CO^* + OH^* \leftrightarrow COOH^* + * \quad (\text{indirect path}, R_{30}-R_{29})$$

$$CO^* + H_2O^* \leftrightarrow COOH^* + H^* \quad (\text{indirect path}, R_{33}-R_{34})$$

$$COOH^* + * \leftrightarrow CO_2^* + H^* (R_{31}-R_{32})$$

play a crucial role in providing the correct *speed* of the WGS chemistry, i.e., the approach to equilibrium with reasonable

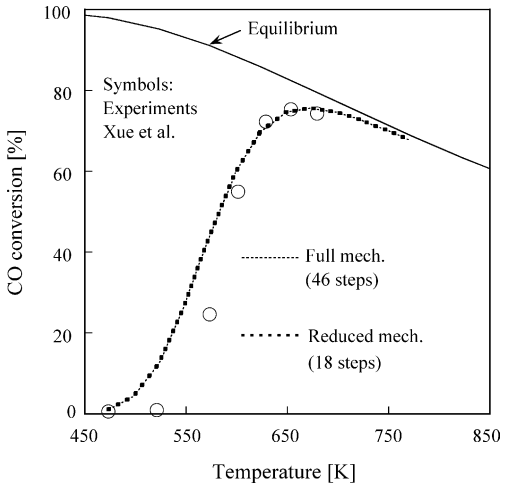

Fig. 2. Comparison of model predictions using the PCA-based 18-step reduced reaction mechanism and the full 46-step reaction mechanism with the experimental data of [22]. The inlet composition is 15% CO, 20% H_2O, 5% CO_2, 5% H_2, and 55% N_2. The equilibrium CO conversion is computed using the GASEQ software [23]. The reduced mechanism matches the performance of the full mechanism over the entire temperature range.

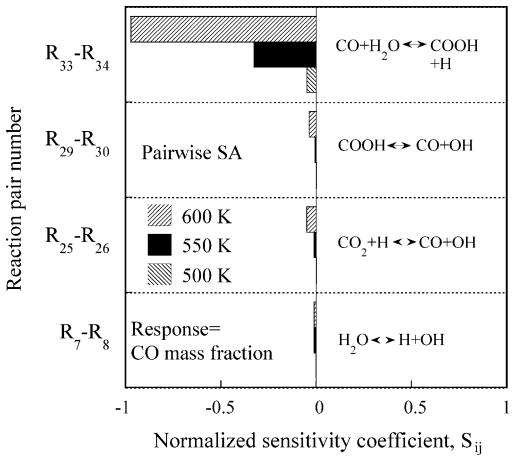

Fig. 3. Sensitivity of CO mass fraction with respect to pre-exponentials at three temperatures indicated. Only the most important reaction pairs of the full reaction mechanism are shown. The reaction $CO^* + H_2O^* \leftrightarrow COOH^* + H^*$ is the most important one.

catalyst surface areas and correct order of magnitude conversion in the kinetically controlled regime [14]. The reaction numbers R_i throughout this paper are those of [14].

The fixed bed reactor experiments of Xue et al. [22] of CO conversion on Pt/ZrO_2 as a function of temperature were simulated using an initial value model (see Fig. 8 in [14]) and the predictions are shown in Fig. 2. The equilibrium CO conversion, computed using the GASEQ software [23], is also shown (solid line). At lower temperatures, the process is kinetically controlled, whereas at higher temperatures, it is equilibrium-limited. The full mechanism captures the WGS data well as shown in Fig. 2. The agreement at low temperatures is not spectacular, but an optimization of the pre-exponentials was not carried out in [14] due to possible uncertainties in the experimental data and the choice of the reactor model. Instead, we maintain flexibility in the mechanism parameters while capturing a multitude of experimental data, e.g., CO oxidation, H_2 oxidation, low-temperature water-promoted CO oxidation, WGS, and PROX.

3.2. Rate-determining step and reduced microkinetic model

SA is carried out on the exit mass fractions of CO, H_2O, CO_2, and H_2 at three temperatures of 500, 550, and 600 K. The pre-exponentials of each reaction pair were decreased by a factor of 2 in carrying out the SA. Fig. 3 shows the most important reaction pairs that control the CO mass fraction (similar sensitivities hold for the other species as well). The magnitude of the sensitivity coefficients varies considerably. It is evident that the CO mass fraction is highly sensitive to the carboxyl formation step (R_{33}–R_{34}), implying that R_{33} is the RDS of the WGS reaction on Pt. The other paths of CO oxidation by OH^*, viz. R_{25}–R_{26} and R_{29}–R_{30} are also slightly important, whereas the direct CO oxidation step ($CO^* + O^* \leftrightarrow CO_2^* + *$) is unimportant. The water decomposition reaction

$$H_2O^* + * \leftrightarrow OH^* + H^* \quad (R_7 - R_8)$$

provides OH^* for the coupling reactions and as a result, it also appears in the SA.

PCA is carried out using the sensitivity information on the exit mass fractions of all four species at three temperatures (500, 550, and 600 K), where moderate to high conversions are observed. The dimensions of the matrix $\mathbf{S}$ are then 12×23. Since there are 23 reversible reactions, there are 23 eigenvalues of the matrix $\mathbf{S}^T\mathbf{S}$. It is found that there is a large disparity in the magnitude of the eigenvalues, as shown in Table 2. In particular, only one eigenvalue is really dominant, with the next two playing a secondary role, and the rest being negligible. Therefore, the absolute values of the elements of the eigenvectors corresponding to the three dominant eigenvalues are considered in selecting the most important reactions, and these are also shown in Table 2.

Using a threshold of 0.2 for the absolute values, only four reaction pairs (R_{33}–R_{34}, R_{25}–R_{26}, R_{29}–R_{30}, and R_7–R_8) entailing part of the carboxyl chemistry and the formation of OH^* are considered as important. The carboxyl formation reaction (R_{33}–R_{34}) clearly dominates all other reactions, as shown from the first eigenvector. Nonetheless, the adsorption–desorption steps of reactants (CO and H_2O) and products (CO_2 and H_2) are also essential for simulations while using an elementary-like surface reaction mechanism in an initial value problem. Therefore, the threshold is reduced to 10^{-5}, so that adsorption–desorption steps are incorporated in the reduced mechanism.

Overall, the reduced, elementary-like mechanism consists of seven species and nine reversible reactions, giving a factor of 2.6 reduction in reaction steps compared to the full

Table 2
Principal component analysis (PCA) results using the full reaction mechanism of [14]

Eigenvalues	First eigenvector	Second eigenvector	Third eigenvector	Reaction pair numbers	Reaction pair
2.1×10^{0}	$\mathbf{-2.6 \times 10^{-4}}$	$\mathbf{2.7 \times 10^{-2}}$	$\mathbf{7.4 \times 10^{-2}}$	$\boldsymbol{R_1}$–$\boldsymbol{R_2}$	$H_2 + 2* \leftrightarrow 2H^*$
3.9×10^{-4}	-1.5×10^{-7}	-6.2×10^{-6}	4.4×10^{-6}	R_3–R_4	$O_2 + 2* \leftrightarrow 2O^*$
3.1×10^{-5}	6.3×10^{-8}	2.3×10^{-6}	-1.6×10^{-6}	R_5–R_6	$OH^* + * \leftrightarrow H^* + O^*$
1.7×10^{-10}	$\mathbf{-1.6 \times 10^{-2}}$	$\mathbf{5.4 \times 10^{-1}}$	$\mathbf{-8.3 \times 10^{-1}}$	$\boldsymbol{R_7}$–$\boldsymbol{R_8}$	$H_2O^* + * \leftrightarrow H^* + OH^*$
1.2×10^{-13}	7.0×10^{-8}	2.8×10^{-6}	-2.5×10^{-6}	R_9–R_{10}	$H_2O^* + O^* \leftrightarrow 2OH^*$
4.8×10^{-16}	3.2×10^{-8}	1.3×10^{-6}	-1.3×10^{-6}	R_{11}–R_{12}	$OH+ * \leftrightarrow OH^*$
Very small eigenvalues	$\mathbf{-3.2 \times 10^{-5}}$	$\mathbf{1.8 \times 10^{-4}}$	$\mathbf{2.8 \times 10^{-4}}$	$\boldsymbol{R_{13}}$–$\boldsymbol{R_{14}}$	$H_2O + * \leftrightarrow H_2O^*$
	3.2×10^{-9}	1.5×10^{-7}	-4.6×10^{-7}	R_{15}–R_{16}	$H + * \leftrightarrow H^*$
	6.1×10^{-8}	2.2×10^{-6}	-1.5×10^{-6}	R_{17}–R_{18}	$O + * \leftrightarrow O^*$
	-5.2×10^{-8}	$\mathbf{-1.6 \times 10^{-4}}$	$\mathbf{-4.7 \times 10^{-5}}$	$\boldsymbol{R_{19}}$–$\boldsymbol{R_{20}}$	$CO + * \leftrightarrow CO^*$
	-1.6×10^{-6}	$\mathbf{-3.8 \times 10^{-5}}$	$\mathbf{1.2 \times 10^{-5}}$	$\boldsymbol{R_{21}}$–$\boldsymbol{R_{22}}$	$CO_2 + * \leftrightarrow CO_2^*$
	5.6×10^{-8}	2.5×10^{-6}	-2.1×10^{-6}	R_{23}–R_{24}	$CO_2^* + * \leftrightarrow CO^* + O^*$
	$\mathbf{-4.7 \times 10^{-2}}$	$\mathbf{-6.4 \times 10^{-1}}$	$\mathbf{-4.8 \times 10^{-1}}$	$\boldsymbol{R_{25}}$–$\boldsymbol{R_{26}}$	$CO_2^* + H* \leftrightarrow CO^* + OH^*$
	-1.8×10^{-7}	-7.1×10^{-6}	5.4×10^{-6}	R_{27}–R_{28}	$COOH + * \leftrightarrow COOH^*$
	$\mathbf{-3.5 \times 10^{-2}}$	$\mathbf{-5.5 \times 10^{-1}}$	$\mathbf{-2.6 \times 10^{-1}}$	$\boldsymbol{R_{29}}$–$\boldsymbol{R_{30}}$	$COOH^* + * \leftrightarrow CO^* + OH^*$
	$\mathbf{-2.2 \times 10^{-4}}$	$\mathbf{-3.7 \times 10^{-3}}$	$\mathbf{9.6 \times 10^{-4}}$	$\boldsymbol{R_{31}}$–$\boldsymbol{R_{32}}$	$COOH^* + * \leftrightarrow CO_2^* + H^*$
	$\mathbf{-1.0 \times 10^{0}}$	$\mathbf{4.0 \times 10^{-2}}$	$\mathbf{4.5 \times 10^{-2}}$	$\boldsymbol{R_{33}}$–$\boldsymbol{R_{34}}$	$CO^* + H_2O^* \leftrightarrow COOH^* + H^*$
	4.3×10^{-8}	1.7×10^{-6}	-1.6×10^{-6}	R_{35}–R_{36}	$CO_2^* + OH^* \leftrightarrow COOH^* + O^*$
	-1.8×10^{-7}	-7.0×10^{-6}	5.4×10^{-6}	R_{37}–R_{38}	$CO_2^* + H_2O^* \leftrightarrow COOH^* + OH^*$
	2.7×10^{-8}	2.4×10^{-7}	2.5×10^{-7}	R_{39}–R_{40}	$HCOO + 2* \leftrightarrow HCOO^{**}$
	-1.5×10^{-7}	-5.8×10^{-6}	4.0×10^{-6}	R_{41}–R_{42}	$CO_2^* + H^* \leftrightarrow COOH^*$
	5.2×10^{-8}	2.0×10^{-6}	-1.8×10^{-6}	R_{43}–R_{44}	$CO_2^* + OH^* + * \leftrightarrow HCOO^{**} + O^*$
	1.2×10^{-8}	-2.0×10^{-7}	4.2×10^{-7}	R_{45}–R_{46}	$CO_2^* + H_2O^* + * \leftrightarrow HCOO^{**} + OH^*$

The dominant eigenvalues are shown in the first column. The eigenvectors corresponding to the three largest eigenvalues of the matrix $\mathbf{S}^{\mathrm{T}}\mathbf{S}$ are shown in columns 2–4, respectively. The corresponding reaction pair numbers and the reactions are shown in the last two columns. Elements indicated in bold meet the cutoff threshold of 10^{-5}.

reaction mechanism. The reduced reaction mechanism along with the rate parameters are listed in Table 3 and is, hereafter, denoted as *PCA-based reduced mechanism*. Model predictions using the PCA-based reduced mechanism, shown in Fig. 2, indicate that the reduced microkinetic model closely follows the full mechanism. It is important to note that the PCA-based reduced mechanism is *thermodynamic consistent* over the entire temperature range, and therefore, it captures the equilibrium-limited regime fairly well.

Table 3
PCA-based, reduced, elementary-like reaction mechanism for the WGS reaction on Pt

No.	Reaction	s (unitless) or A (s^{-1})	β	E (kcal/mol)
R_1	$H_2 + 2* \rightarrow 2H^*$	1.29×10^{-1}	0.858	0
R_2	$2H^* \rightarrow H_2 + 2*$	7.95×10^{12}	−0.001	$22.24 - 2.56(T/T_o) - 6\theta_H$
R_7	$H_2O^* + * \rightarrow H^* + OH^*$	9.36×10^{12}	−0.118	$17.31 + 0.38(T/T_o) + 12.03\theta_O + 1.15\theta_H + 12.49\theta_{OH} - 10.33\theta_{H_2O}$
R_8	$H^* + OH^* \rightarrow H_2O^* + *$	9.99×10^{12}	−1.049	$13.98 - 0.92(T/T_o) - 20.97\theta_O - 1.85\theta_H - 12.49\theta_{OH} + 17.15\theta_{H_2O}$
R_{13}	$H_2O + * \rightarrow H_2O^*$	1.08×10^{-1}	1.162	0
R_{14}	$H_2O^* \rightarrow H_2O + *$	2.03×10^{12}	1.372	$10 - 2.5R(T - T_o) - 2.5\theta_{H_2O} + 25\theta_{OH}$
R_{19}	$CO + * \rightarrow CO^*$	1.00×10^{0}	0.000	0
R_{20}	$CO^* \rightarrow CO + *$	5.66×10^{15}	−0.500	$40 - 2R(T - T_o) - 15\theta_{CO}$
R_{21}	$CO_2 + * \rightarrow CO_2^*$	1.95×10^{-1}	0.250	0
R_{22}	$CO_2^* \rightarrow CO_2 + *$	3.63×10^{12}	−0.250	Max $(3.6 - 2R(T - T_o),0)$
R_{25}	$CO_2^* + H^* \rightarrow CO^* + OH^*$	8.03×10^{8}	−0.531	$5.95 - 0.28(T/T_o) + 14.4\theta_O - 1.5\theta_H - 10.89\theta_{H_2O} + 4.33\theta_{CO}$
R_{26}	$CO^* + OH^* \rightarrow CO_2^* + H^*$	1.25×10^{9}	0.531	$18.85 - 0.38(T/T_o) - 18.6\theta_O + 1.5\theta_H + 14.11\theta_{H_2O} - 10.67\theta_{CO}$
R_{29}	$COOH^* + * \rightarrow CO^* + OH^*$	8.43×10^{8}	0.024	$5.38 + 7.82 \times 10^{-3}(T/T_o) + 14.4\theta_O - 10.89\theta_{H_2O} + 4.33\theta_{CO}$
R_{30}	$CO^* + OH^* \rightarrow COOH^* + *$	1.19×10^{9}	−0.024	$19.41 - 0.67(T/T_o) - 18.6\theta_O + 14.11\theta_{H_2O} - 10.67\theta_{CO}$
R_{31}	$COOH^* + * \rightarrow CO_2^* + H^*$	1.06×10^{11}	0.549	$1.22 - 3.6 \times 10^{-2}(T/T_o) + 1.5\theta_H$
R_{32}	$CO_2^* + H^* \rightarrow COOH^* + *$	9.45×10^{10}	−0.549	$2.34 - 0.62(T/T_o) - 1.5\theta_H$
R_{33}	$CO^* + H_2O^* \rightarrow COOH^* + H^*$	1.10×10^{11}	0.492	$23.59 + 1.36 \times 10^{-3}(T/T_o) + 1.17\theta_H + 12.49\theta_{OH} - 1.24\theta_{H_2O} - 7.5\theta_{CO}$
R_{34}	$COOH^* + H^* \rightarrow CO^* + H_2O^*$	9.07×10^{10}	−0.492	$6.25 - 0.62(T/T_o) - 1.83\theta_H - 12.49\theta_{OH} + 1.24\theta_{H_2O} + 7.5\theta_{CO}$

The modified Arrhenius expression, $k = \frac{A}{\sigma^{n-1}}\left(\frac{T}{T_o}\right)^{\beta} e^{-E/RT}$ or $k = \frac{s}{\sigma^{n}}\sqrt{\frac{RT}{2\pi M}}\left(\frac{T}{T_o}\right)^{\beta} e^{-E/RT}$ is used for computing the rate constant k. Here, A is the pre-exponential, s the sticking coefficient, σ the site density, n the reaction order, β the temperature exponent, E activation energy, R the ideal gas constant, and T is the absolute temperature. T_o is taken as 300 K. The last column shows fits of activation energies for ease of use (see text). If any activation energy is negative, it is set to zero, and its reverse activation energy is set to be the heat of reaction. Under our conditions θ_O is practically zero.

3.3. Development of a one-step, analytical rate expression

Here we attempt to further reduce the PCA-based reduced mechanism into an analytical one-step rate expression. Using the steps in Table 3, the following steady state balances are obtained for the surface species:

$$\frac{d\theta_H}{dt} = 2r_1 - 2r_2 + r_7 - r_8 - r_{25} + r_{26} + r_{31} - r_{32} + r_{33} - r_{34} = 0, \quad (2)$$

$$\frac{d\theta_{OH}}{dt} = r_7 - r_8 + r_{25} - r_{26} + r_{29} - r_{30} = 0, \quad (3)$$

$$\frac{d\theta_{H_2O}}{dt} = -r_7 + r_8 + r_{13} - r_{14} - r_{33} + r_{34} = 0, \quad (4)$$

$$\frac{d\theta_{CO}}{dt} = r_{19} - r_{20} + r_{25} - r_{26} + r_{29} - r_{30} - r_{33} + r_{34} = 0, \quad (5)$$

$$\frac{d\theta_{CO_2}}{dt} = r_{21} - r_{22} - r_{25} + r_{26} + r_{31} - r_{32} = 0, \quad (6)$$

$$\frac{d\theta_{COOH}}{dt} = -r_{29} + r_{30} - r_{31} + r_{32} + r_{33} - r_{34} = 0, \quad (7)$$

where r stands for the reaction rate and θ for the surface species coverage (fraction of occupied surface sites). The overall site conservation equation is

$$\theta_H + \theta_{OH} + \theta_{H_2O} + \theta_{CO} + \theta_{CO_2} + \theta_{COOH} + \theta_* = 1, \quad (8)$$

where '*' denotes vacancies.

In order to simplify the above expressions, terms in species and site balances are compared to each other. At high temperatures (equilibrium-limited regime), all reaction pairs are in equilibrium. The reversibility of various steps at lower temperatures is assessed by defining the PE ratio φ as

$$\varphi = \frac{r_f}{r_f + r_b}, \quad (9)$$

where r_f and r_b indicate the forward and backward reaction rates. A value of $\varphi = 0.5$ indicates that a reaction is in PE, whereas when φ deviates from 0.5, a reaction is not in PE. Values of φ at three temperatures are shown in Fig. 4a. It is evident that the adsorption–desorption steps of H_2O, CO, and CO_2 are in PE. At higher temperatures, the H_2 adsorption–desorption step R_1–R_2, the water decomposition step R_7–R_8, and the carboxyl decomposition step R_{31}–R_{32} approach PE, but they slightly deviate from PE at lower temperatures. Other surface reactions, viz. the CO oxidation paths (R_{25}–R_{26}, R_{29}–R_{30}, and R_{33}–R_{34}) are not in PE at higher temperatures of the kinetically controlled regime, indicating that the RDS is possibly one or a combination of these reactions. Comparison of the rates of these CO oxidation paths shows that the net rate of carboxyl formation by H_2O^* (R_{33}–R_{34}) is much higher (by approximately one to two orders of magnitude) than that of the parallel paths by OH^* (R_{25}–R_{26} or R_{29}–R_{30}), indicating that the WGS on Pt occurs mainly via R_{33}, corroborating with the aforementioned SA and PCA results about R_{33} being the RDS. This is mainly due to relative abundance of H_2O^* participating in R_{33} compared to OH^* involved in the other oxidation steps (both of these species are in relatively low fractions on the surface and their ratio is strongly temperature dependent) as well as due to a larger pre-exponential of R_{33} than those of R_{26} and R_{30}.

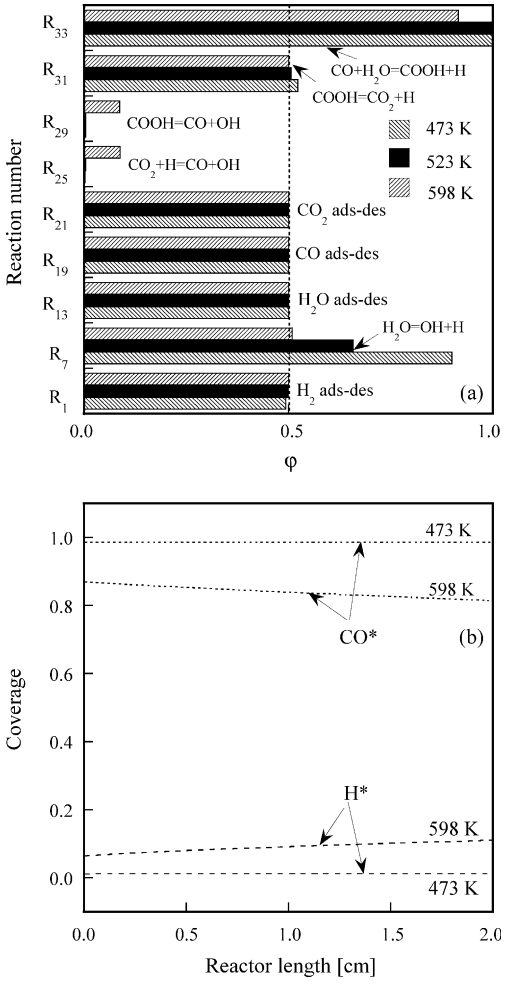

Fig. 4. (a) Partial equilibrium (PE) ratio at three sample temperatures indicated. The adsorption–desorption steps of CO, H_2O, and CO_2 are in PE. (b) dominant coverages at two temperatures as a function of reactor length. CO^* is the most abundant reactive intermediate, followed by H^*.

The coverages of dominant species over the reactor length are shown in Fig. 4b. CO^* is the MARI at all temperatures. The H^* coverage is small (up to ~0.1), but is significantly higher than those of the remaining species. Therefore, Eq. (8) can be significantly simplified. Fig. 5a and b show the RPA at a sample temperature of 548 K for CO and H_2O consumption paths, respectively. The contribution of adsorption–desorption steps is neglected in calculating the relative importance of reactions consuming the surface species. It is evident that R_{33} dominates over the rest of the CO^* consumption pathways.

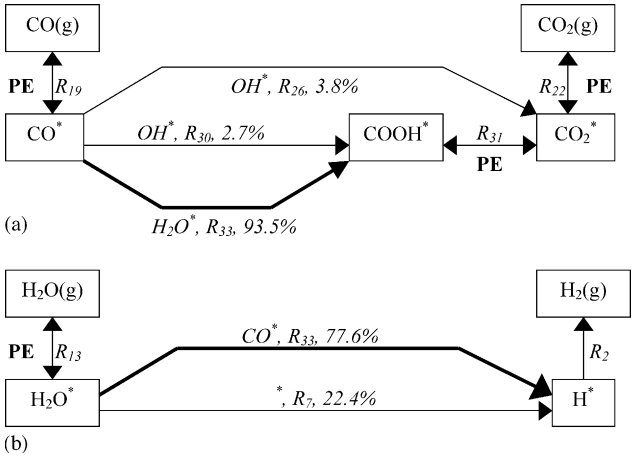

Fig. 5. Panels (a) and (b) show the reaction path analysis for CO and H_2O consumption pathways, respectively, at 548 K. The contribution of fast adsorption–desorption steps is not taken into account to highlight the relative importance of slow reaction pathways. The reaction $CO^* + H_2O^* \rightarrow COOH^* + H^*$ (shown with bold arrows) dominates.

In deciding the importance of rate and coverage terms in Eqs. (2)–(8), a threshold of 1% is used. It should be noted that in comparison to the large adsorption–desorption rates, r_{33} is just over the threshold limit only at low temperatures and therefore, it is omitted from computing the species coverages (see below for details). The simplified balances are

$$\frac{d\theta_H}{dt} = 2r_1 - 2r_2 + r_{31} - r_{32} + r_{33} = 0, \quad (2')$$

$$\frac{d\theta_{OH}}{dt} = r_7 - r_8 - r_{26} - r_{30} = 0, \quad (3')$$

$$\frac{d\theta_{H_2O}}{dt} = r_{13} - r_{14} = 0, \quad \therefore\ r_{13} = r_{14}, \quad (4')$$

$$\frac{d\theta_{CO}}{dt} = r_{19} - r_{20} = 0, \quad \therefore\ r_{19} = r_{20}, \quad (5')$$

$$\frac{d\theta_{CO_2}}{dt} = r_{21} - r_{22} = 0, \quad \therefore\ r_{21} = r_{22}, \quad (6')$$

$$\frac{d\theta_{COOH}}{dt} = -r_{31} + r_{32} + r_{33} = 0, \quad \therefore\ r_{31} - r_{32} = r_{33}, \quad (7')$$

$$\text{and } \theta_H + \theta_{CO} + \theta_* = 1. \quad (8')$$

Eqs. (4′)–(6′) are consistent with the PE analysis shown in Fig. 4a. From the reduced species balances (Eqs. (4′)–(6′)), the coverages of H_2O, CO, and CO_2 are derived as follows:

$$\theta_{H_2O} = K_{13} C_{H_2O} \theta_*, \quad (10)$$

$$\theta_{CO} = K_{19} C_{CO} \theta_*, \quad (11)$$

$$\text{and } \theta_{CO_2} = K_{21} C_{CO_2} \theta_*, \quad (12)$$

where K is the equilibrium constant and C is the concentration of the gas phase species in mol/cm^3. Substituting Eq. (7′) into Eq. (2′), one gets

$$2r_1 - 2r_2 + 2r_{33} = 0 \quad \text{or} \quad r_1 - r_2 + r_{33} = 0. \quad (2'')$$

Using Eqs. (2″), (10), and (11), the coverage of H is derived as

$$\theta_H = \sqrt{\frac{k_1 C_{H_2} + k_{33} K_{19} C_{CO} K_{13} C_{H_2O}}{k_2}}\,\theta_*, \quad (13)$$

where k denotes rate constant. For all practical purposes, the magnitude of r_{33} is small compared to r_1 (the maximum value of r_{33}/r_1 is ∼0.03 over the entire temperature range). Therefore, Eq. (13) could further be simplified as

$$\theta_H = \sqrt{K_1 C_{H_2}}\,\theta_*. \quad (13')$$

Using Eqs. (3′), (10), (11), and (13′), the coverage of OH is determined as

$$\theta_{OH} = \frac{k_7 K_{13} C_{H_2O}}{k_8 \sqrt{K_1 C_{H_2}} + (k_{26} + k_{30}) K_{19} C_{CO}}\,\theta_*. \quad (14)$$

Using Eqs. (7′), (10)–(12), and (13′), the coverage of COOH can be derived as

$$\theta_{COOH} = \frac{k_{32}\sqrt{K_1 C_{H_2}} K_{21} C_{CO_2} + k_{33} K_{19} C_{CO} K_{13} C_{H_2O}}{k_{31}}\,\theta_*. \quad (15)$$

Again, for all practical purposes, the magnitude of r_{33} is small compared to r_{32} (a maximum value of r_{33}/r_{32} is ∼0.09 over the entire temperature range). Therefore, Eq. (15) could be simplified as

$$\theta_{COOH} = \frac{\sqrt{K_1 C_{H_2}} K_{21} C_{CO_2}}{K_{31}}\,\theta_*. \quad (15')$$

Using Eq. (8′), the coverage of vacancies is finally determined as

$$\theta_* = \frac{1}{1 + \sqrt{K_1 C_{H_2}} + K_{19} C_{CO}}. \quad (16)$$

Since the adsorption–desorption steps of CO, H_2O, and CO_2 are in PE, the net rate of di-hydrogen, σ_{H_2}, is used to determine the rate of the overall reaction. Using Eq. (2″), we get

$$\sigma_{H_2} = r_1 - r_2 = -r_{33} = -k_{33}\theta_{CO}\theta_{H_2O}. \quad (17)$$

The net rates of other species can be represented in terms of the net H_2 rate using the stoichiometry of the overall WGS reaction ($CO + H_2O \leftrightarrow CO_2 + H_2$) as

$$\sigma_{H_2O} = -\sigma_{H_2}, \quad \sigma_{CO} = -\sigma_{H_2} \quad \text{and} \quad \sigma_{CO_2} = \sigma_{H_2}. \quad (18)$$

The rate expression for the forward WGS reaction is then given as

$$\sigma_{WGS} = \frac{k_{33} K_{19} K_{13} C_{CO} C_{H_2O}}{\left(1 + \sqrt{K_1 C_{H_2}} + K_{19} C_{CO}\right)^2}. \quad (19)$$

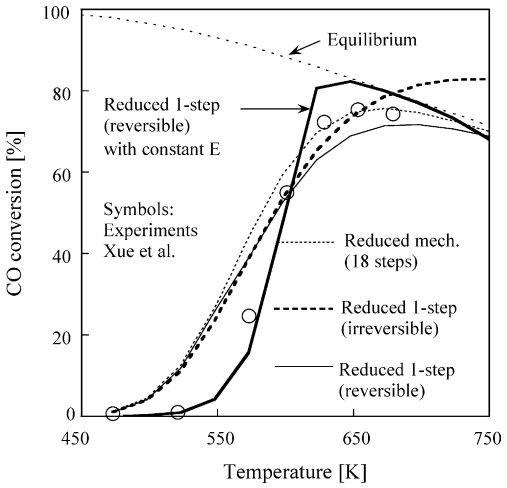

Fig. 6. Comparison of the irreversible one-step rate expression (Eq. (19)), the reversible one-step rate expression (Eq. (21)), a reversible one-step rate expression with constant activation energies E, the reduced microkinetic model (Table 3), and the experimental data. The irreversible rate expression captures the kinetically controlled regime, but fails to capture the equilibrium-limited regime. The reversible expressions behave fairly well.

The activation energies of the rate constants in these expressions are calculated using the semi-empirical unity bond index-quadratic exponential potential (UBI-QEP) theory [24,25] using the heats of chemisorption of species as an input. Furthermore, statistical mechanics is employed to account for the temperature dependence of the heats of chemisorption. The coverage and temperature dependence of the heats of chemisorption translates into coverage and temperature dependent activation energies as discussed in detail in [26]. For simplicity, here the activation energies are fitted as a linear function of temperature and coverages, and the fits are shown in Table 3. For ease of use, these fits are used in computing effective reaction rate constants whenever a one-step rate expression (Eq. (19) or its reversible form Eq. (21) (see next)), is used.

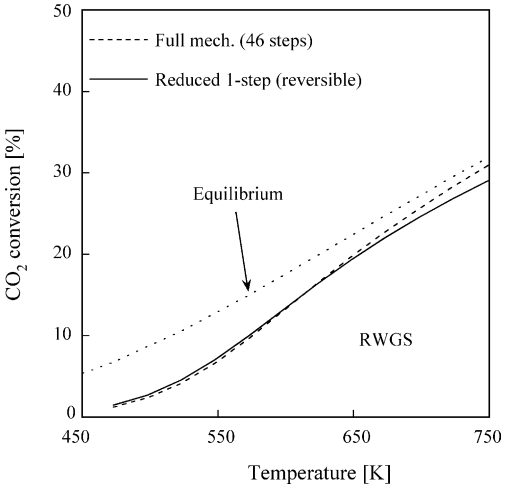

Fig. 7. Comparison of the reversible one-step rate expression (Eq. (21)) with the full reaction mechanism for the RWGS reaction. The inlet composition is 20% CO_2, 25% H_2, and 55% N_2. The reversible expression retains the features of the full mechanism reasonably well.

The performance of the one-step rate expression (Eq. (19)) against the PCA-based reduced mechanism is depicted in Fig. 6 (thick, dashed line). It is observed that the analytical expression shows similar predictions with those of the reduced microkinetic model in the low temperature, kinetically controlled regime. However, since the one-step rate expression does not account for backward reactions (the RWGS reaction) at high temperatures, it is *thermodynamically inconsistent* and fails to capture the equilibrium-limited regime. These deviations are magnified as temperature increases.

In order to develop a one-step rate expression that is reversible, a similar analysis is performed for the RWGS reaction. An inlet composition of 20% CO_2, 25% H_2, and 55% N_2 is considered. Fig. 7 shows the predictions using the full reaction mechanism along with the equilibrium CO_2 conversion computed using the GASEQ software [23]. The full mechanism predictions converge to the equilibrium conversion in the equilibrium-limited regime at high temperatures. Pairwise SA (not shown) in the kinetically controlled regime (at 500, 550, and 600 K) indicates that the CO_2 conversion is sensitive to the reaction R_{33}–R_{34} ($CO^* + H_2O \leftrightarrow COOH^* + H^*$), in analogy to the WGS reaction. Using RPA, it is found that R_{34} is not in PE for the RWGS reaction. Analytical expressions for different surface coverages are then derived (not shown) as done above, and the rate of RWGS is given as

$$\sigma_{\mathrm{RWGS}} = \frac{k_{34}K_{21}K_1K_{31}^{-1}C_{\mathrm{CO_2}}C_{\mathrm{H_2}}}{\left(1+\sqrt{K_1C_{\mathrm{H_2}}}+K_{19}C_{\mathrm{CO}}\right)^2}. \tag{20}$$

Subtracting Eq. (20) from Eq. (19), the net rate of the WGS reaction is given as

$$\sigma_{\mathrm{net}} = \frac{k_{33}K_{19}K_{13}C_{\mathrm{CO}}C_{\mathrm{H_2O}} - k_{34}K_{21}K_1K_{31}^{-1}C_{\mathrm{CO_2}}C_{\mathrm{H_2}}}{\left(1+\sqrt{K_1C_{\mathrm{H_2}}}+K_{19}C_{\mathrm{CO}}\right)^2}, \tag{21}$$

The performance of the reversible one-step rate expression (Eq. (21)) is also depicted in Figs. 6 and 7 (thin, solid line). The reversible one-step rate expression is *thermodynamically consistent* and retains the features of the microkinetic models fairly well.

While employing this one-step rate expression, one needs to solve for surface coverages using, for example, a Newton's algorithm. Due to omission of low order of magnitude terms from the site conservation equation (see Eqs. (8) and (8′)), convergence can become an issue. Note that this is a well-known problem in chemistry reduction carried out in flame modeling. In such cases, one can employ a more detailed rate expression,

considering all surface species in the site conservation, given by

$$\sigma_{\text{net}} = \frac{k_{33}K_{19}K_{13}C_{\text{CO}}C_{\text{H}_2\text{O}} - k_{34}K_{21}K_1K_{31}^{-1}C_{\text{CO}_2}C_{\text{H}_2}}{\left(1 + \sqrt{K_1C_{\text{H}_2}} + \frac{k_7K_{13}C_{\text{H}_2\text{O}}}{k_8\sqrt{K_1C_{\text{H}_2}} + (k_{26}+k_{30})K_{19}C_{\text{CO}}} + K_{13}C_{\text{H}_2\text{O}} + K_{19}C_{\text{CO}} + K_{21}C_{\text{CO}_2} + \sqrt{K_1C_{\text{H}_2}}K_{21}K_{31}^{-1}C_{\text{CO}_2}\right)^2}. \quad (22)$$

It is useful to introduce the effective forward reaction rate constant

$$k_{\text{eff}} = \frac{k_{33}K_{19}K_{13}}{(1 + \sqrt{K_1C_{\text{H}_2}} + K_{19}C_{\text{CO}})^2}. \quad (23)$$

In passing we should note that Eq. (21) could also had been postulated by subtracting σ_{RWGS} from σ_{WGS} so that at equilibrium, the net rate σ_{net} is equal to zero. This would have led to the following postulate

$$\sigma_{\text{net}} = k_{\text{eff}}C_{\text{CO}}C_{\text{H}_2\text{O}} - \frac{k_{\text{eff}}}{K_{\text{eq}}}C_{\text{CO}_2}C_{\text{H}_2}, \quad (24)$$

which is in fact equivalent to Eq. (21). Comparison of Eqs. (24) and (21) indicates that the equilibrium constant of the WGS reaction is indeed related to elementary-like reaction steps appearing in Eq. (21) as

$$K_{\text{eq}} = K_{33}K_{31}K_{19}K_{13}K_{21}^{-1}K_1^{-1}. \quad (25)$$

This can easily be shown by considering the linear combination of the corresponding elementary reactions.

Eq. (21) was developed at a particular inlet composition. To exploit the validity of this expression, simulations were performed for inlet CO:H_2O ratios ranging from 1:6 to 6:1. The analytical expression gives fair agreement with the full mechanism as shown in Fig. 8a. Fig. 8b shows similar behavior for different inlet flow rates. Furthermore, the effect of catalyst area per unit reactor volume over the range of 5–50,000 cm^{-1} and the effect of inlet CO_2 over the range of 0–30% (by compensating the inlet N_2 in the range of 60–30%) are also reasonably well captured (not shown). Overall, the one-step analytical expression is able to maintain reasonable accuracy.

3.4. Reaction orders

The effective forward reaction rate constant in Eq. (22) and the net reaction rate given by Eq. (21) indicate that the effective reaction orders can vary significantly with operating conditions. Let α, β, γ, and δ be the reaction orders with respect to CO, H_2O, CO_2, and H_2, respectively, according to the notation of Table 1. Overall the predicted reaction orders can explain the experimentally observed reaction orders despite experiments being conducted on various catalysts with different conditions. For example, the reaction order with respect to H_2O in Table 1 varies between 0 and 1. Our expression predicts $\beta = 1$, except under excess H_2O conditions, where $\beta \sim 0$. Reaction orders with respect to H_2 and CO are more interesting. Due to the stronger adsorption of CO on Pt compared to H_2, at low temperatures corresponding to low conversions, the term $K_{19}C_{\text{CO}}$ dominates in the denominator of k_{eff} and $\alpha = -1$ and $\gamma \sim 0$. However, this occurs only under practically non-measurable conversions ($<\sim$1%). At higher temperatures where measurable conversions are seen, inhibitory kinetics is still important but the resistance is not as large, so the effective reaction order for CO is expected to be much larger than -1 (possibly positive order kinetics).

In comparison with limited published work on WGS reaction on Pt, under CO saturation conditions, negative order kinetics for CO was hypothesized as a possibility by

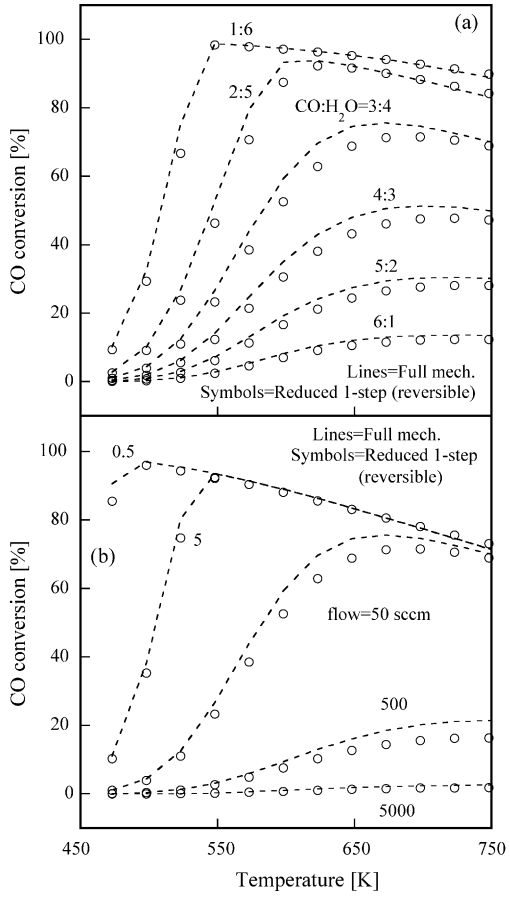

Fig. 8. Validity of the reversible one-step rate expression (symbols) given by Eq. (21) for changes of inlet composition and flow rate against the full reaction mechanism predictions (dashed lines). The one-step expression is fairly accurate over a wide range.

Wheeler et al. [2]. Jacobs et al. [27] carried out experiments on Pt/CeO_2 under high H_2O/CO conditions. Using DRIFTS, they concluded that at high temperatures, the surface coverage of CO is low and the effective CO reaction order is one. Our simulations under such conditions also indicate that the coverage of CO^* decreases as a function of increasing temperature. However, further experiments at different conditions are needed to delineate the effective reaction orders and test our theoretical predictions.

3.5. Coverage independent activation energies

Since the activation energies are coverage dependent, one needs to solve for the surface coverages at each reactor location using, for example, Newton's method. We have also explored the possibility of setting constant, averaged coverages with representative values of $\theta_H = 0.08$, $\theta_{CO} = 0.84$ and $\theta_* = 0.08$, which result in coverage independent activation energies (see Table 3). The performance of the one-step rate expression (Eq. (21)) with such constant activation energies is shown in Fig. 6 (thick, solid line). The predictions are in reasonable agreement without fine-tuning the values of coverages. It should be noted that the improved performance of the reduced mechanism stems from cancellation of errors resulting from the elimination of reactions based on a certain threshold.

3.6. The effect of uncertainty in reaction rate constants on inferring the rate-determining step

Based on our analysis, reaction R_{33} ($CO^* + H_2O^* \rightarrow COOH^* + H^*$) is the RDS in the WGS process. A rate expression discussed by Wheeler et al. [2] based on Langmuir–Hinshelwood kinetics postulated the lumped reaction $CO^* + H_2O^* \rightarrow CO_2^* + H_2^*$ as the RDS. This is indeed consistent with our a posteriori analysis of our full microkinetic model where actual numbers have instead been used for all steps.

A comparison of activation energies of different CO^* consumption pathways (R_{26}, R_{30}, and R_{33}) on Pt shows that the activation energies of R_{26} and R_{30} vary between 8 and 10 kcal/mol whereas that of R_{33} between 16 and 18 kcal/mol as the temperature increases from 200 to 350 °C (see Table 3). On the other hand, the pre-exponential of R_{33} is larger than of those of R_{26} and R_{30}, compensating in part for the larger activation energy and resulting in reaction rate constants that differ by one to two orders of magnitude. Since the typical uncertainty in activation energy estimates using the UBI-QEP method is of the order of 5 kcal/mol, it is worth investigating the effect of such uncertainty on the RDS predictions, especially given the relatively low temperatures encountered in WGS chemistry. We conducted numerical simulations, where the reaction pair R_{33}–R_{34} was removed from the full reaction mechanism and we found that the predicted catalyst activity decreases significantly. However, by decreasing the activation energies of R_{25}–R_{26} and R_{29}–R_{30} by 2–3 kcal/mol, the catalyst activity can be recovered and the experimental data can be captured well. SA in this case indicates that the water decomposition reaction R_7 is the most important reaction, followed by the CO^* consumption pathways R_{26} and R_{30}. Therefore, uncertainties in rate parameters *can* affect, at least on Pt, the relative importance of reactions and hence, the RDS of the WGS process on Pt cannot unambiguously be determined. Further work is needed to fully delineate this mechanistic issue.

4. Conclusions

In this paper, a recently developed elementary-like, comprehensive reaction mechanism for the WGS reaction on Pt is analyzed. A reduced microkinetic model is first derived using sensitivity and principal component analyses. Based on reaction path analysis and small parameter asymptotics, a simple one-step analytical rate expression is developed for the WGS and the RWGS reactions. The reversible, one-step rate expression captures the kinetically controlled and equilibrium-limited regimes fairly well over a wide range of conditions (inlet compositions, flow rates, and catalyst area). Our results indicate that the WGS chemistry on Pt is complex but can indeed be represented with a simple one-step reaction with the coupling reaction describing the formation of carboxyl ($CO^* + H_2O^* \rightarrow COOH^* + H^*$) being the rate-determining step. Our analysis highlights that the effective reaction rate constant is concentration dependent, and as a result, the effective reaction orders in each reactant can be more complex than first-order, depending on the operating conditions. Finally, competing paths for CO^* oxidation on Pt by OH^* instead of H_2O^* cannot completely be ruled out as being important (with the H_2O^* decomposition being the rate-determining step), due to the relatively small differences in activation energies of these parallel oxidation paths.

Acknowledgments

We acknowledge partial support of this research by the donors of the Petroleum Research Fund, administered by the American Chemical Society and by the U.S. Department of Energy, under Award No. DE-FG02-03ER15468. However, any opinions, findings, conclusions, or recommendations expressed herein are those of the authors and do not necessarily reflect the views of the DOE.

References

[1] C. Rhodes, B. Peter Williams, F. King, G.J. Hutchings, Catal. Commun. 3 (2002) 381.

[2] C. Wheeler, A. Jhalani, E.J. Klein, S. Tummala, L.D. Schmidt, J. Catal. 223 (2004) 191.
[3] B.I. Whittington, C.J. Jiang, D.L. Trimm, Catal. Today 26 (1995) 41.
[4] T. Bunluesin, R.J. Gorte, G.W. Graham, Appl. Catal. B: Environ. 15 (1998) 107.
[5] S. Hilaire, X. Wang, T. Luo, R.J. Gorte, J. Wagner, Appl. Catal. A: Gen. 215 (2001) 271.
[6] X. Wang, R.J. Gorte, Appl. Catal. A: Gen. 247 (2003) 157.
[7] D. Andreeva, V. Idakiev, T. Tabakova, L. Ilieva, P. Falaras, A. Bourlinos, A. Travlos, Catal. Today 72 (2002) 51.
[8] D. Wolf, M. Barre-Chassonnery, M. Hohenberger, A. van Veen, M. Baerns, Catal. Today 40 (1998) 147.
[9] G. Jacobs, E. Chenu, P.M. Patterson, L. Williams, D. Sparks, G. Thomas, B.H. Davis, Appl. Catal. A: Gen. 258 (2004) 203.
[10] Q. Fu, H. Saltsburg, M. Flytzani-Stephanopoulos, Science 301 (2003) 935.
[11] A. Luengnaruemitchai, S. Osuwan, E. Gulari, Catal. Commun. 4 (2003) 215.
[12] T. Shido, Y. Iwasawa, J. Catal. 141 (1993) 71.
[13] P. Panagiotopoulou, D.I. Kondarides, J. Catal. 225 (2004) 327.
[14] A.B. Mhadeshwar, D.G. Vlachos, J. Phys. Chem. B 108 (2004) 15246.
[15] S.R. Deshmukh, A.B. Mhadeshwar, D.G. Vlachos, Ind. Eng. Chem. Res. 43 (2004) 2986.
[16] S.R. Deshmukh, A.B. Mhadeshwar, M. Lebedeva, D.G. Vlachos, Int. J. Multiscale Comp. Eng. 2 (2004) 221.
[17] E.V. Rebrov, M.H.J.M. de Croon, J.C. Schouten, Chem. Eng. J. 90 (2002) 61.
[18] D.G. Vlachos, Chem. Eng. Sci. 51 (1996) 3979.
[19] S. Vajda, P. Valko, T. Turanyi, Int. J. Chem. Kinet. 17 (1985) 55.
[20] S. Vajda, T. Turanyi, J. Phys. Chem. 90 (1986) 1664.
[21] A.B. Mhadeshwar, D.G. Vlachos, 2005, in press.
[22] E. Xue, M.O. Keeffe, J.R.H. Ross, Catal. Today 30 (1996) 107.
[23] C. Morley, GASEQ: Chemical equilibria in perfect gases, Version 0.75b, taken from http://www.c.morley.ukgateway.net/.
[24] E. Shustorovich, H. Sellers, Surf. Sci. Rep. 31 (1998) 1.
[25] E. Shustorovich, Adv. Catal. 37 (1990) 101.
[26] A.B. Mhadeshwar, H. Wang, D.G. Vlachos, J. Phys. Chem. B 107 (2003) 12721.
[27] G. Jacobs, L. Williams, U. Graham, G.A. Thomas, D.E. Sparks, B.H. Davis, Appl. Catal. A: Gen. 252 (2003) 107.
[28] S.-J. Kim, I.-S. Byun, H.-Y. Han, H.-L. Ju, S.H. Lee, J.-G. Choi, Appl. Catal. A: Gen. 234 (2002) 35.
[29] D.C. Grenoble, M.M. Estadt, D.F. Ollis, J. Catal. 67 (1981) 90.
[30] C.T. Campbell, K.A. Daube, J. Catal. 104 (1987) 109.
[31] Y. Li, Q. Fu, M. Flytzani-Stephanopoulos, Appl. Catal. B: Environ. 27 (2000) 179.
[32] R.L. Keiski, T. Salmi, P. Niemisto, J. Ainassaari, V.J. Pohjola, Appl. Catal. A: Gen. 137 (1996) 349.
[33] N.A. Koryabkina, A.A. Phatak, W.F. Ruettinger, R.J. Farrauto, F.H. Ribeiro, J. Catal. 217 (2003) 233.
[34] R.L. Keiski, O. Desponds, Y.-F. Chang, G.A. Somorjai, Appl. Catal. A: Gen. 101 (1993) 317.